EarthArXiv Coversheet

Unified Granular Intrusion Dynamics for Planetary Materials

John G. Ruck[1], Shravan Pradeep[1,2], John C. Bush[3], Eric D. Sigg[2], Feifei Qian[3], Douglas J. Jerolmack[1,2]

[1]University of Pennsylvania, Department of Earth and Environmental Science, [2]University of Pennsylvania, Department of Mechanical Engineering and Applied Mechanics, [3]University of Southern California, Department of Electrical and Computer Engineering

Email

Corresponding author: sediment@sas.upenn.edu

Peer-review statement

This manuscript is in first-round review at *PNAS* and has not been peer-reviewed.

Unified Granular Intrusion Dynamics for Planetary Materials

John G. Ruck[a], Shravan Pradeep[a,b], John C. Bush[c], Eric D. Sigg[b], Feifei Qian[c], and Douglas J. Jerolmack[a,b,2]

This manuscript was compiled on September 16, 2025

Granular friction μ is a sensitive and poorly understood function of packing fraction ϕ. Every granular material has a distinct critical volume fraction ϕ_c that delineates two mechanical deformation modes – compaction for $\phi < \phi_c$, and dilation for $\phi > \phi_c$. Here we examine the relation(s) between friction and packing fraction, using quasi-static penetration tests in materials ranging from glass beads to highly heterogeneous lunar regolith simulant. Noncohesive materials collapse onto a master curve that relates changes in friction to the distance from ϕ_c, confirming that the handoff from compaction to dilation is a phase transition. The mechanical distinction between compaction and dilation regimes is highlighted with the addition of cohesive dust – relevant for lunar regolith – which has little effect for $\phi < \phi_c$, but drastically enhances strength for $\phi > \phi_c$. Our simple model improves predictions of granular resistance to intrusion, which can help to explore and manipulate soils on Earth and regolith on other planets. A reanalysis of Apollo-era lunar penetration tests demonstrates the promise of our approach.

granular friction | planetary material | phase transition | robotic intruder

Significance Statement

Loose sand compacts under foot, and hard sand dilates. This simple difference is key to understanding how soil reacts to loads such as feet, wheels and buildings, and how it fails. Using a robotic intruder, we determine the critical packing that separates compaction from dilation for sand, glass beads, and even lunar soil simulant. Whether digging in a sandbox or on the Moon, soils follow the same rule: strength depends only on how close the material is to its critical packing. Sprinkle in cohesive dust, like the coating on lunar grains, and dilating soils get a surprising strength boost. By determining material-specific critical packing, we show how experiments on Earth can be used to interpret soil behavior on the Moon.

As robots and humans explore planetary surfaces, their wheels and feet continuously intrude complex granular materials (1–5). Lunar regolith, for example, is likely the most heterogeneous granular material ever encountered by humans (6–9). Inadequate understanding of regolith rheology can lead to critical sampling and mobility failures; for instance, the inability of the Mars Insight Mole to penetrate regolith was due to unanticipated cohesion (10), and the Mars Exploration Rover Spirit ended its mission due to embedding in a loose patch of sand (11). Future missions that endeavor to construct with and excavate lunar (12, 13) and Martian (14) regolith will require (i) an improved understanding of how material properties control rheology, and (ii) mechanical sensors to inform rheologic models. This paper takes an important step toward these goals.

There are quantitative and qualitative changes in the response of a granular material to stress, depending on the volume fraction ϕ. Consider walking on a beach. Far from the water's edge, the sand feels soft and our foot sinks in. Closer to the water's edge, where sand has recently been sheared by waves, the substrate feels hard and sand bulges up around our footprint (Fig. 1A). In both cases, the sand deforms under a load; however, the 'soft' sand compacts (Fig. 1B) while the 'hard' sand dilates. Critical State Soil Mechanics (CSSM) is a framework that describes how the effective friction μ of a granular material and its volume fraction ϕ change under strain. The 'critical state' is defined as the condition of perfect plasticity, where sheared soil achieves a constant volume fraction ϕ_c and friction μ_c associated with failure. For $\phi < \phi_c$, soil is relatively weak and compacts under strain; for $\phi > \phi_c$, soil is relatively strong and must dilate to accommodate strain. Thus, the friction of soil at a given ϕ depends on the distance from the critical state ϕ_c, where ϕ_c and μ_c vary with material properties (15, 16):

$$\mu = \mu_c + f(\phi - \phi_c). \quad [1]$$

Andreotti et al. (17) summarize several different functional forms for Eq. 1, representing various levels of complexity and assumptions in CSSM. The simplest models assume that the relative change in friction away from ϕ_c is symmetric. In experiments that our work here directly builds on, however, careful penetration tests into glass beads by Schröter et al. (18) revealed an asymmetric behavior. Beginning from an air-fluidized bed with the loosest possible packing (ϕ_{min}), they found that penetration resistance increased slowly with increasing ϕ up to a critical value ϕ_c, beyond which resistance increased rapidly. The authors proposed that compaction and dilation represent distinctly different mechanical responses, and that the handoff at ϕ_c is a phase transition. It is unclear whether and how the

Author affiliations: [a]Department of Earth and Environmental Science, University of Pennsylvania, Philadelphia, PA 19104, USA; [b]Department of Mechanical Engineering and Applied Mechanics, University of Pennsylvania, Philadelphia, PA 19104, USA; [c]Department of Electrical and Computer Engineering, University of Southern California, Los Angeles, CA 90089, USA

Conceptualization: J.G.R. and D.J.J.; Funding Acquisition: F.Q. and D.J.J.; Formal Analysis: J.G.R., S.P., and D.J.J.; Data Curation: J.G.R. and S.P.; Methodology: J.G.R., J.C.B., E.S., and D.J.J.; Investigation: J.G.R. and J.C.B.; Visualization: J.G.R., S.P., and J.C.B.; Resources: J.G.R., E.S., F.Q., and D.J.J.; Writing-original draft: J.G.R.; Writing-review and editing: J.G.R., S.P., and D.J.J.

The authors declare that they have no competing interests.

[2]To whom correspondence should be addressed. E-mail: sediment@sas.upenn.edu

findings from Schröter et al. (18) can be generalized to more complex granular materials, or incorporated into CSSM.

Here we perform penetration experiments on a variety of cohesionless granular materials — glass beads, natural sand, and lunar regolith simulant — to examine the inter-relations of penetration resistance, volume fraction, and material properties. Each material has its own critical values for ϕ_c and μ_c that separate compaction and dilation. We find that these data can be collapsed, however, to reveal two distinct functional relations between friction and the distance from the critical state — one for compaction, and another for dilation. Adding cohesive dust to the lunar simulant highlights the mechanical differences between compaction and dilation; we observe little effect in the compaction regime, but drastic strengthening in the dilation regime. Finally, we demonstrate that these findings extend to scales and conditions relevant for lunar exploration, by conducting experiments in the NASA Ames SSERVI test bed and using those results to reinterpret penetration tests conducted in the Apollo era on the Moon's surface.

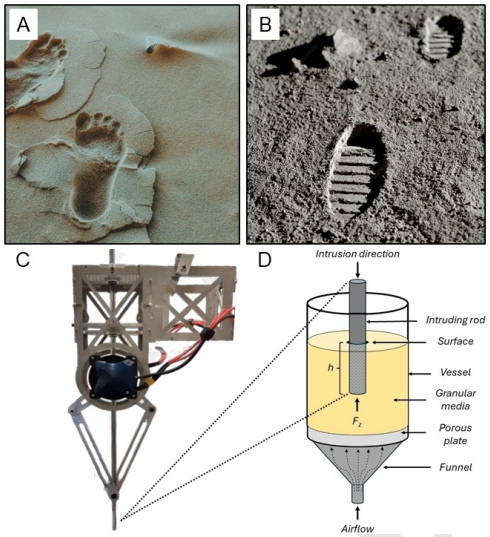

Fig. 1. Compaction and dilation in granular materials with robotic intruder and apparatus used for penetration experiments. (A) Bare footprint impression in sand, showing dilation about the perimeter of the impression. Image credit CC0, via Pexels. (B) Astronaut footprints into lunar regolith on the Moon's surface from the Apollo 11 Mission, exhibiting compaction of loose material. Image credit: Detlev van Ravenswaay. (C) Robotic intruder leg used in experiments actuated with two direct-drive gearless motors that obtain mechanically sensitive and time-efficient measurements of the strength of granular materials. (D) Sketch of the experimental air-fluidizing apparatus.

Results

Conceptual and theoretical framework. Slow (quasi-static) penetration tests are a robust and portable method for determining granular material properties that are relevant for modeling intruder-ground interactions. Granular resistance to penetration is insensitive to both angle (19) and speed beyond a shallow surficial depth (20, 21). More, we have found that penetration tests are more reproducible in the field than shear tests (22). For purely frictional (noncohesive) granular materials, there is an initial depth $h_0 \approx R_e$ over which a well-developed granular wedge forms beneath the intruder; beyond this depth there is a steady-state regime in which the force on the intruder F_z increases linearly with depth h following a modified Archimedes law (23, 24). Here $R_e \equiv \sqrt{A/\pi}$ is equivalent intruder radius and A is the cross-sectional area of the intruder. The Archimedes model can be recast in terms of a dimensionless penetration depth, $\tilde{h} \equiv h/R_e$, and dimensionless pressure, $\tilde{p}_u \equiv F_z/(\rho_b g R_e A)$:

$$\tilde{p}_u = K\tilde{h} + \tilde{p}_0, \qquad [2]$$

where $\rho_b = \rho_p \phi$ is bulk density and ρ_p is particle density, and g is gravity. The parameter K is reminiscent of a dimensionless stiffness, and indeed simple terramechanics models portray granular materials as a one-way spring (25, 26). K is a material property that is proportional to the effective friction μ of the granular material (23, 27), and $\tilde{p}_0$ is the dimensionless pressure at the transition to the linear regime.

In this study we aim to determine how granular friction changes with volume fraction, over the widest range of ϕ possible. In principle, the lowest possible volume fraction ϕ_{min} is associated with random loose pack; in this state, grains can support their own weight but will deform under any load. The highest possible packing fraction ϕ_{max} is random close pack; in this regime, particles are jammed at all stresses. In the framework of CSSM, ϕ evolves under strain γ toward the critical value ϕ_c; a typical relation is (17):

$$\frac{d\phi}{d\gamma} = -\phi \tan(n(\phi - \phi_c)). \qquad [3]$$

The term $n(\phi - \phi_c)$ represents a dilatancy angle, describing the change in material thickness (negative for compaction and positive for dilation) associated with a given horizontal strain; n is an order one empirical parameter (28). With some assumptions (Supp. Info., Section S1) we can derive a volumetric strain γ^*:

$$\gamma^* \equiv \frac{\phi - \phi_c}{\phi}. \qquad [4]$$

We can think of γ^* as the volumetric deformation that the material must undergo to achieve the critical state.

In a penetration experiment, the intruder is continuously encountering new material in the bulk that will be deformed until it reaches the critical state – unless the grains are already prepared at $\phi = \phi_c$. We define the relative change in friction, compared to the critical state, as $\mu^* \equiv (\mu - \mu_c)/\mu_c$; from CSSM we expect that this quantity is some function of γ^*. Recasting friction in terms of penetration resistance – assuming $K \propto \mu$ (19) – and defining $K^* \equiv (K - K_c)/K_c$, we anticipate that:

$$K^* = A\,|\gamma^*|^n\,, \qquad [5]$$

where A and n are empirical parameters to be determined from experiment. We take the absolute value of γ^* so that Eq. 5 is defined for arbitrary values of n. The penetration experiments we describe below seek to develop a generalized functional form for Eq. 5 that can describe various frictional granular materials.

Penetration experiments in frictional materials. We perform vertical penetration tests into various granular materials at a constant speed $v = 2$ cm/s, well within the quasistatic regime defined by the grain settling speed $v_c = \sqrt{2gd} \sim 10$

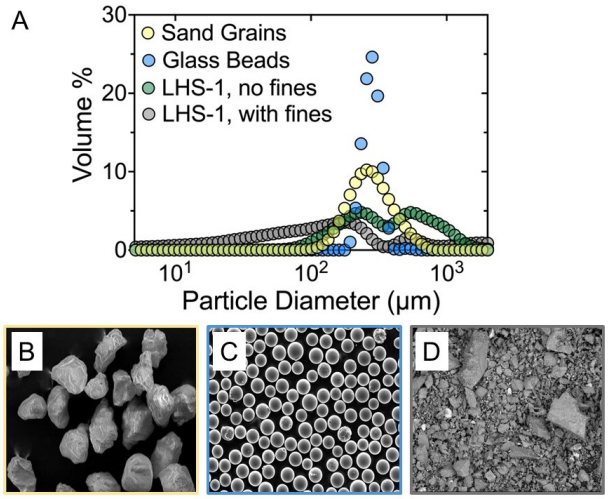

Fig. 2. Granular material properties. (A) Particle size distribution for each material. (B) SEM image of silica sand. Image credit: Poppe et al., 2021. (C) SEM image of glass beads. Image credit: Krzizek & Schöppe, 2010. (D) SEM image of LHS-1. Image credit: NASA JSC.

cm/s, where d is particle diameter (21, 23, 29). Our intruder, described previously (27), is an aluminum cylinder ($R_e = 0.635$ cm) driven vertically by a single-leg direct-drive robot (Fig. 1C) that simulates a robotic leg (22). The intruder is driven to a maximum depth $h = 10$ cm or a maximum force $F_z = 40$ N, which are limits of our apparatus (see Methods). We examine three frictional (cohesionless) granular materials: polydisperse silica sand (Fig. 2B) and monodisperse glass beads (Fig. 2C) that both have a modal diameter of $d \approx 250\mu$m (Fig. 2A); and the highly heterogeneous lunar highlands regolith simulant LHS-1 (Fig. 2D) (30), sieved at 75μm to remove the cohesive silt and dust fraction (Fig. 2A). We later re-introduce this fine fraction, to examine the influence of cohesive particles on penetration resistance. Granular beds are carefully prepared in a custom air-fluidized chamber (Fig. 1D) (diameter = 21.6 cm). For each test, particles are first entirely fluidized to create a reproducible initial condition. The loosest volume fraction ϕ_{min} is achieved by abruptly ceasing the fluidizing airflow. To achieve more dense packings up to ϕ_c, airflow is pulsed over a period of time until a desired ϕ is achieved (31). To drive the system to packings $\phi > \phi_c$, we tap the vessel with a rubber mallet; the maximum packing density ϕ_{max} is set by the saturation of volume fraction under this tapping. Before a test, all disturbances are stopped and ϕ is determined by measuring the height of the granular bed. This technique allowed us to create granular packs at discrete increments of ϕ over the following ranges: $0.55 \leq \phi \leq 0.615$ for sand, $0.56 \leq \phi \leq 0.625$ for glass beads, and $0.50 \leq \phi \leq 0.58$ for sieved LHS-1. For some experiments we used a laser profilometer to measure the topography of the bed surface in the vicinity of the intruder, following a penetration test (see Methods).

We first examine the behavior of silica sand, an idealized but 'natural' frictional material. Data confirm that penetration resistance increases linearly with depth following Eq. 2 for all volume fractions (Fig. 3A. Fig. S1), which allows us to extract penetration resistance K as a function of ϕ (Fig. 3B). As expected, K increases monotonically with ϕ over the entire range. The relation appears to be bipartite: K increases slowly up to a volume fraction that we infer to be the critical value $\phi_c \approx 0.59$, beyond which K increases more rapidly (Fig. 3B). Topographic profiles confirm that ϕ_c is associated with a transition from compaction to dilation (Fig. 3B, inset, Fig. S2). At $\phi = \phi_{min}$, there is a conical depression around the intruder indicating significant compaction. At $\phi = \phi_{max}$, there is a significant topographic bulge around the intruder showing dilation. At $\phi = \phi_c$, there is essentially no topographic change away from the intruder suggesting no volume change. These results confirm previous observations (32) and support the notion that the handoff from compaction to dilation is a phase transition.

The other noncohesive granular materials exhibit qualitatively similar behavior to sand, though with significant differences in the magnitudes of K and μ_c. Glass beads have the lowest friction, as expected, and the transition from compaction to dilation occurs at $\phi_c \approx 0.595$ (Fig. 4A) – comparable to our sand experiments, and nearly identical to the value determined by Schröter (18) who also used glass beads. Lunar simulant, by far the most heterogeneous material in terms of particle size and shape, exhibits the greatest range in friction and packing fraction. Both $\phi_{min} \approx 0.50$ and $\phi_c \approx 0.53$ are significantly lower than the other materials (Fig. 4A); this is likely due to the extreme angularity of LHS-1 particles, which constrains rolling/sliding motions and allows grains to withstand a compressive load at a much lower volume fraction (30, 33). In the dilation regime ($\phi > \phi_c$), we observe that K increases more rapidly with ϕ for LHS-1 than the other materials. We speculate that the extreme stiffening in this regime is also because of angularity, through its constraints on grain motions that facilitate dilation. Can all of these effects really be captured in a simple universal constitutive equation, like Eq. 5? The surprising answer is yes. Using the experimentally-determined values for the critical state, K_c and ϕ_c, we find that data from all three materials collapse when recast in terms of K^* and γ^* (Fig. 4B). This collapse reveals the stark asymmetry of the compaction and dilation regimes moving away from the critical state. Materials weaken slowly and sublinearly as ϕ decreases from ϕ_c toward ϕ_{min}. In contrast, there is a rapid superlinear strengthening as ϕ increases from ϕ_c toward ϕ_{max}.

Effects of cohesion. The regolith encountered in Apollo missions is notorious for its dust content, which is both abrasive and sticky (9, 34). The (unsieved) lunar simulant LHS-1, with a grain-size range $0.04\mu\text{m} < d < 1000\mu$m, is meant to mimic the regolith properties determined from samples of the lunar highlands (30). Here we re-introduce the fine fraction – particles $< 75\mu$m – to examine if and how cohesive silt and dust influence the mechanical properties of this complex material. With the fines, the minimum packing fraction is significantly reduced to $\phi_{min} \approx 0.45$; this is an expected effect of cohesion, which provides an extra constraint to grain motion (35, 36). The magnitude of K in the compaction regime, however, is comparable to LHS-1 without fines. This suggests that the modest cohesion from fines has little influence on material resistance to a compressive load. Indeed, the functional dependence of K^* on γ^*, determined for frictional materials above, can be

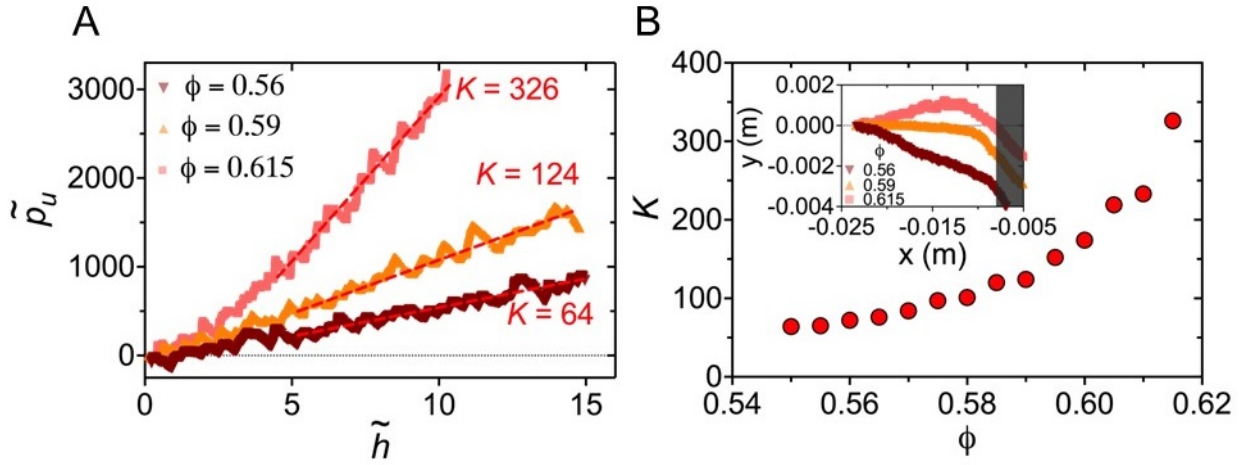

Fig. 3. Results from sand experiments. (A) Force profiles for sand at ϕ_{min}, ϕ_c, and ϕ_{max}, each profile is an average of four intrusion tests. The red fit lines are corresponding values of K. (B) Values for K (fitted lines in 3A) and the associated ϕ. Inset: surface displacement profiles. The horizontal dotted line at y = 0 m represents the granular surface. The transparent grey bar symbolizes the intruder location. Negative y values reflect material that has dilated and extended above the surface, while positive y measures correspond to material that has been compacted. Values of x approaching 0 are closer to the center of intrusion.

applied to the compaction regime of this frictional-cohesive material. The same is not true for dilation. Interestingly, there is little change in either ϕ_c or ϕ_{max} with the addition of fines. The rate of increase of K with ϕ as $\phi \to \phi_{max}$, however, is dramatically enhanced (Fig. 5C).

Relevance for lunar activities. Future missions to the Moon plan to excavate, transport, and even build with lunar regolith (13). Such activities will not only require knowledge of material rheology; they will alter the mechanical properties of lunar regolith through compaction and dilation. Do results from our well-controlled and highly idealized laboratory experiments extrapolate to conditions for planetary exploration? As a first step toward answering this question, we conducted penetration tests in the NASA Ames SSERVI test bed (37). This 19 x 4 m box was filled to a depth of 0.3 m with LHS-1 including fines (Fig. 5A). Because this is a large and mixed use facility, the preparation of the granular bed is uncontrolled. We performed mechanical manipulation of the regolith in localized regions of the bed, using a shovel to either 'fluff' the bed to a relatively loose state or 'tamp' the bed to a relatively compact state. We call the loose and compacted states ϕ_{min} and ϕ_{max}, respectively, although we did not attempt to measure the packing fractions for any of the regolith in the SSERVI test bed. We observe qualitative and quantitative differences in the penetration force curves of loose vs. compacted regolith (Fig. 5B). Loose material is relatively weak and the curves are convex; resistance increases slowly at first, and the transient pre-linear regime extends up to relatively large depths $\tilde{h} \geq 4$. Compacted material is stronger and the curves are concave; resistance increases rapidly at first, and the transient pre-linear regime is significantly smaller, $\tilde{h} \approx 1$.

We now conduct a reanalysis of available data from penetration tests performed on the Moon's surface. The goal is to determine if and how our simulant experiments in the SSERVI test bed help to interpret lunar regolith. Several Apollo missions included manual cone penetration tests conducted by astronauts (9, 38–41), with maximum relative depths that were much larger than our experiments. Some of these tests suffered equipment failures, and others did not have sufficient documentation; we deemed two vertical force profiles from Apollo 15, however, to be of sufficient quality to reanalyze here (Fig. S3). We also reanalyze published data from four shallow penetration tests from the Lunokhod 1 rover (9, 42, 43), which achieved maximum relative depths that were smaller than our experiments. We nondimensionalize pressure $\tilde{p}_u$ and depth $\tilde{h}$ in the same way as our experiments; this accounts not only for the varying intruder geometries and bulk densities associated with the lunar tests, but also for the reduced gravity of the Moon compared to Earth. We first observe that the Apollo 15 curves contain a feature that others do not: several sharp jumps in resistance, which have been attributed to layering of lunar regolith at these sites (38) (Fig. 5D). There are no layers in the SSERVI test bed, of course; for Lunokhod sites we do not know if the regolith there is not layered, or just that tests were insufficiently deep to reveal layering. Ignoring the layers, we observe something remarkable: all of the lunar penetration curves are bounded by the SSERVI test bed data. In other words, the loose and compacted LHS-1 experiments account for the full range of regolith strengths observed in the available Moon data. Most lunar curves are convex and similar to the ϕ_{min} data from LHS-1; they appear to represent the pre-linear regime for loose regolith that is compacting, i.e., $\phi < \phi_c$. Anecdotally, footprints and treads observed in lunar missions are consistent with loose (and cohesive) regolith that compacts under load. One Lunokhod curve hews closely to the ϕ_{max} data from LHS-1, indicating compacted regolith that dilates under load. We do not have sufficient knowledge of site-specific conditions to test the veracity of this assessment. More broadly, we acknowledge that LHS-1 is not representative of the range of compositions of lunar regolith; and that the limited Moon penetration data here are likely not representative of the range of lunar regolith behaviors. More, our experiments reported here do not account for the potential effects of lunar vacuum, which can alter inter-particle forces substantially (44–46). Thus,

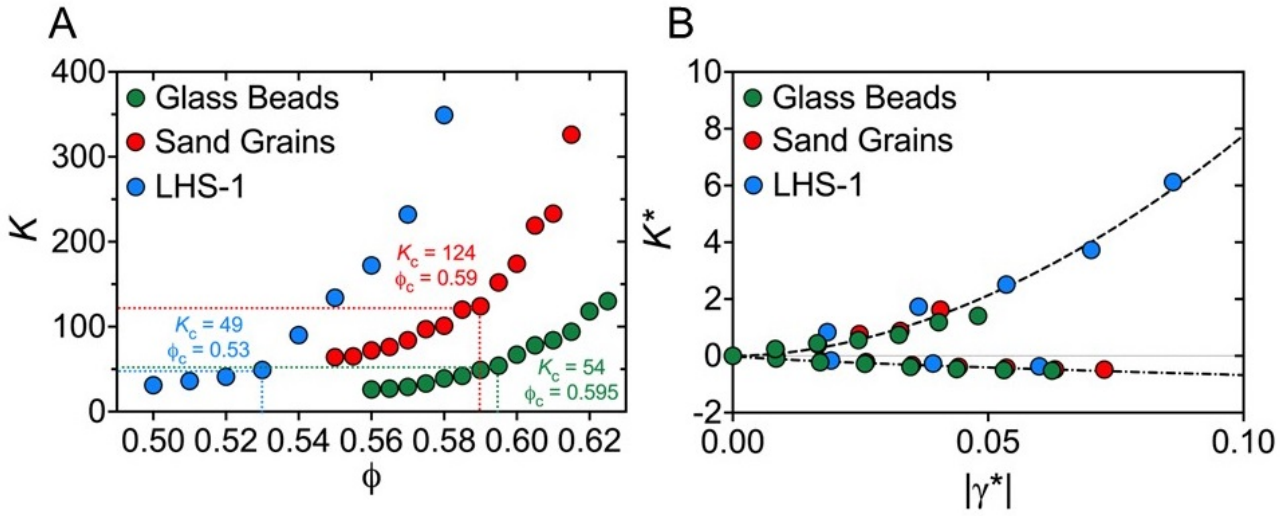

Fig. 4. Unifying material strength as a function of the distance from critical. (A) Values of K and the associated ϕ for each material. (B) The critical point where K^* , γ^* = 0 delineates and collapses the intrusion dynamics of disparate samples into two regimes: dilation where K^* is positive, and compaction where K^* is negative. The dashed lines are power law fits of the form $K^* = A|\gamma^*|^n$ where A is a prefactor that sets the overall magnitude of the deviation from critical behavior, and where n is an exponent that describes how sharply K diverges or vanishes upon the approach to ϕ_c.

we caution against quantitative comparison or extrapolation of our experiments to the Moon. Nonetheless, these results give us confidence that simulant tests on Earth, appropriately nondimensionalized, are useful for anticipating the response of lunar regolith. In addition, the large differences in penetration curves between loose and compacted LHS-1 simulant – both qualitative and quantitative – highlight the importance of preparation protocol for terramechanics and locomotion experiments.

Discussion and Implications

Qualitatively, the increase of friction with packing fraction is easy to understand. From an Archimedes perspective, increasing ϕ increases the bulk density and therefore the resisting force (Eq. 2). At a granular scale, the coordination number Z – the average number of contacts that a grain has with its neighbors – increases monotonically with ϕ (47); this results in an increase in effective friction (48, 49). The asymmetry in the compaction vs. dilation regimes, however, cannot be explained by density/volume fraction arguments. The granular response to compression is distinct from that of shear. Qualitatively, granular contacts can be maintained under compression, but shear produces 'severe particle rearrangements' (50). Quantitatively, the bulk (compressional) modulus and the shear modulus both increase monotonically with Z but follow distinct relations; the bulk modulus is the larger of the two at relatively low Z (or ϕ), while the shear modulus becomes larger at high Z (or ϕ) (17, 51, 52). In our penetration experiments, shear and compression are both at play and cannot be isolated from each other. A reasonable mechanical interpretation, however, is that resistance is dominated by compression for the compaction regime ($\phi < \phi_c$), while resistance in dilation ($\phi > \phi_c$) is dominated by shear. This interpretation is bolstered by the addition of cohesive fine materials to LHS-1. In mixed soils, the normal stress is borne by a skeleton of coarse frictional grains, while fine cohesive grains provide resistance to tensile stress (28, 53, 54). Indeed, this principle is used to optimize construction with geomaterials (54). The addition of fines did not change penetration resistance in the compaction regime of LHS-1, supporting the contention that resistance is predominantly compressive (Fig. 5C). Fines greatly enhanced resistance in the dilation regime, because cohesion provides an additional constraint to the particle rearrangements induced by shear (Fig. 5C).

The relations that we find between penetration resistance and packing fraction are entirely consistent with the CSSM framework, and experimental findings from other approaches such as shear boxes and tri-axial tests (17, 55, 56). What is new then, and how is it useful? The collapse of penetration resistance data, for disparate frictional materials, reveals a universal behavior of granular friction. The details of varying material properties (size and shape) only enter the picture through two empirical parameters, K_c and ϕ_c (Fig. 4B). The results are useful because penetration tests like ours are a robust and low-cost method for *in-situ* measurement of soil and regolith mechanics (22, 27, 57, 58) that can be deployed rapidly and frequently on vehicles and rovers. Using the relations found here, robotic penetrometers could be deployed to learn about regolith mechanics and even composition – and also use this information to inform locomotion (26, 31, 59–61). The translation of simulant test bed experiments to actual penetration tests on the Moon's surface demonstrates that this approach holds promise. Legged robots are currently being developed with capabilities that enable each leg to operate as an independent rheometer, making each step an experiment (62).

The addition of cohesion breaks the purely frictional rheology model, as the dilation regime of LHS-1 with fines cannot be collapsed onto the same curves as the frictional materials; but we believe that this is a feature, not a bug. Granular admixtures abound in nature, where cohesive materials – water, ice, clays, dust, organic matter, and salt crusts, to name a few – are mixed with frictional grains (27, 63–

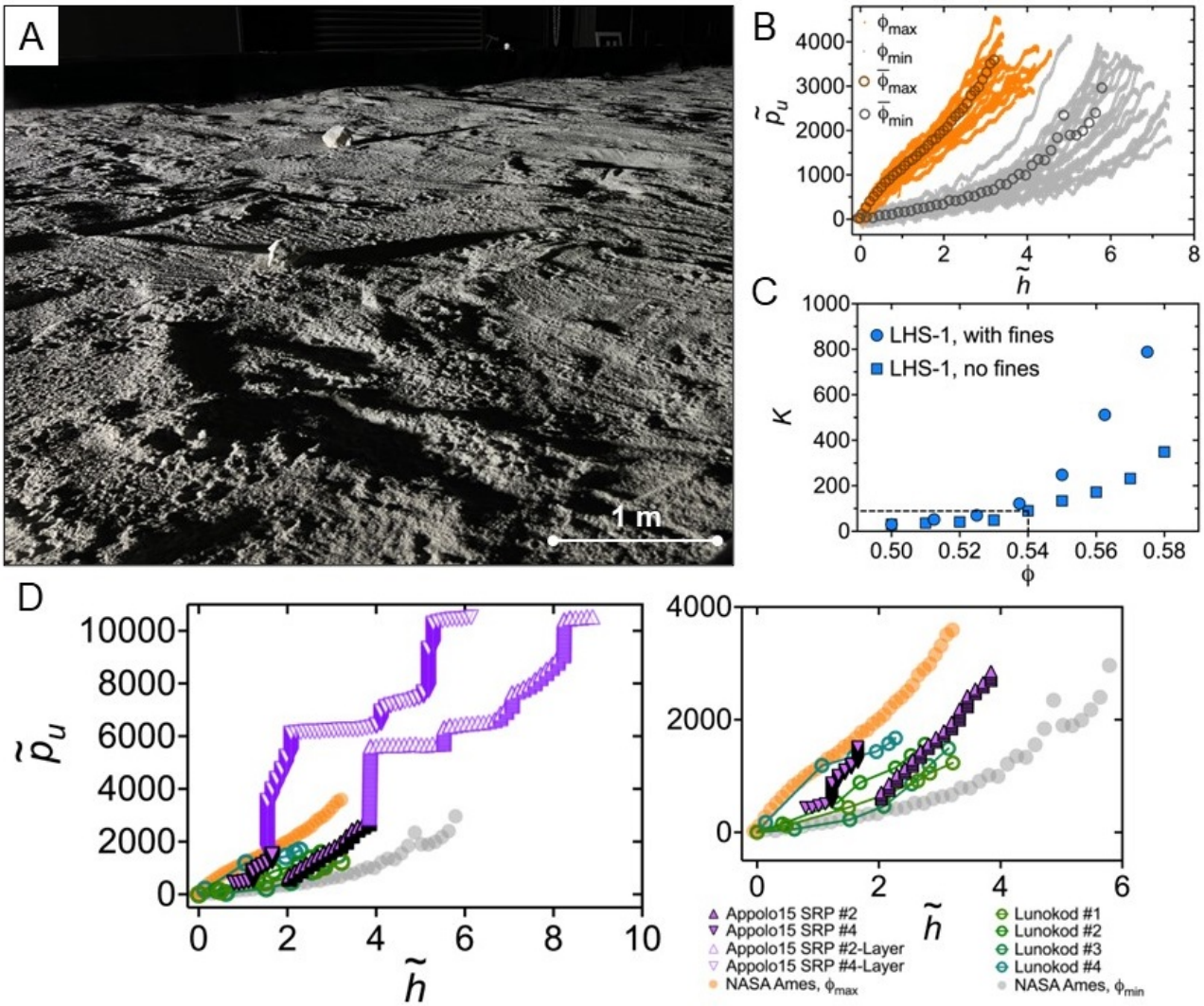

Fig. 5. Intrusion experiments in the lab and on the Moon. (A) NASA Ames SSERVI test bed. (B) Dimensionless pressure-depth plots from intrusion experiments in LHS-1 at ϕ_{min} (gray) and ϕ_{max} (orange), with averages of each shown in hollow scatter, at NASA Ames. (C) Stiffness of LHS-1 with fines and without fines plotted against corresponding volume fraction. The shared critical point is delineated by the black dotted line. (D) Reinterpreted data from penetration tests on the lunar surface recorded by Lunokhod I and the Apollo 15 SRP, and the NASA Ames test bed. The layered zones of the Apollo 15 profiles (left) are lighter and transparent; right plot is a zoom in, with layered zones removed for comparison of lunar and lab data.

65). The penetration curves of these admixtures will reveal new features that indicate a more complex material. Models that describe these materials will require new parameters. But we envision a near future where mobile robots, endowed with the capability to determine regolith composition and mechanical behavior, will be able to learn how material controls rheology – simply by walking (66).

Materials and Methods

We intrude into our selected granular media at a constant speed $v = 2$ cm/s, ensuring that the intruder does not sink through the bed due to its own weight and that deformation is not influenced by inertial effects. The intruder body is an aluminum cylinder with a 1.27 cm diameter. The intruder is driven vertically into the bed with a single-leg direct-drive robot (Fig. 1C), actuated by two high-torque brushless DC motors, with position control enabled by a v3.6 ODrive motor controller. During each intrusion test, the intruder is directed to penetrate to a depth h_{max} of 10 cm, and is then returned back to an idle starting position above the bed. At a resolution of 300 Hz, we obtain an accurate and continuous measurement of the external forces in the vertical plane throughout the entire intrusion depth using the motor's current draw and leg kinematics (67, 68). For each measure of ϕ, we intrude four times and average the data to produce force/depth profiles (Fig. 3A, Fig. S1).

We use a custom fluidizing air-chamber described in (27) (Fig. 1D). For the frictional materials – sand, glass beads, and the LHS-1 sieved to remove particles smaller than 75μm – we fluidize the bed prior to each test to achieve the desired ϕ, while also guaranteeing a 'reset' initial and reproducible bed condition (27). We are able to tune ϕ by applying a flow upward through a rigid porous plate sufficient to completely fluidize the pack. The ϕ_{min} limit is achievable by completely fluidizing the system and then abruptly turning off the air flow and allowing grains to settle. Driving the system towards ϕ_c requires decreasing and pulsing the air flow over a period of time, which acts to slowly compact the pack. Further compaction to ϕ_{max} required mechanically agitating the grains by tapping the vessel.

The unsieved LHS-1 has a typical grain size range of $0.04 \leq d \leq 1000$ μm. We were unable to use the fluidization chamber for this material due to static cling of dust to the walls, spontaneous segregation of fine grains making the pack nonuniform, and ejection of fine grains by airflow. Preparation instead involved slowly sifting the LHS-1 into an acrylic cylinder (diameter = 19.15 cm) and mechanically agitating the chamber by tapping with a rubber mallet to achieve the desired ϕ. Due to our concerns about homogeneity and reproducibility of this preparation protocol, we prepared the bed three times for each ϕ and averaged the results.

Lastly, we use a wenglor MLSL132 laser line profilometer positioned normal to the surface to measure topographic change (Fig. S2) related to a material's proximity to ϕ_c. Inspiration for this technique comes from studies on penetration of projectiles into granular targets and granular impact (32, 69).

Data Availability

The data required to reproduce figures in this study have been deposited in the Zenodo repository (DOI: 10.5281/zenodo.15610745). All other data needed to evaluate the conclusions in the paper are present in the paper and Supplementary Information.

ACKNOWLEDGMENTS. We are grateful for our sources of funding, including: NASA PSTAR (80NSSC22K1313), NASA LuSTR (80NSSC24K0127), NSF MRSEC (NSF-DMR-1720530).

References

1. A Ellery, *Planetary Rovers: Robotic Exploration of the Solar System.* (Springer, Berlin, Heidelberg), (2016).
2. Y Gao, ed., *Contemporary Planetary Robotics: An Approach Toward Autonomous Systems.* (Wiley-VCH, Berlin), (2016).
3. TdJ Mateo Sanguino, 50 years of rovers for planetary exploration: A retrospective review for future directions. *Robotics Auton. Syst.* **94**, 172–185 (2017).
4. A Thoesen, H Marvi, Untethered locomotion strategies for marsupial and non-marsupial robotic systems. *Curr. Robotics Reports* **2**, 239–248 (2021).
5. JL Callas, Mars exploration rover spirit end of mission report, (NASA Jet Propulsion Laboratory, California Institute of Technology, Pasadena, CA), Technical Report JPL D-75240 (2015).
6. WD Carrier, Particle size distribution of lunar soil. *J. Geotech. Geoenvironmental Eng.* **129**, 956–959 (2003).
7. J Graf, Lunar soils grain size catalog (1993).
8. WD Carrier, J Mitchell, A Mahmood, The nature of lunar soil. *ASCE J. Soil Mech. Foundations Div.* **99** (1973).
9. W Carrier, G Olhoeft, W Mendell, in *Lunar Sourcebook: A User's Guide to the Moon.* (Cambridge University Press), (1991).
10. T Spohn, et al., The insight hp3 penetrator (mole) on mars: Soil properties derived from the penetration attempts and related activities. *Space Sci. Rev.* **218**, 72 (2022).
11. R Arvidson, et al., Spirit mars rover mission: Overview and selected results from the northern home plate winter haven to the side of scamander crater. *J. Geophys. Res.* **115** (2010).
12. RP Mueller, Lunar base construction planning in *Earth and Space 2022: Engineering for Extreme Environments.* (American Society of Civil Engineers, Denver, CO), (2022).
13. National Aeronautics and Space Administration, Artemis plan: Nasa's lunar exploration program overview, (NASA), Technical report (2020).
14. National Aeronautics and Space Administration, Expanding the horizons of mars science: A plan for a sustainable science program at mars, 2024–2044, (NASA Science Mission Directorate), Technical report (2024).
15. H Liu, E Song, H Ling, Constitutive modeling of soil-structure interface through the concept of critical state soil mechanics. *Mech Res Commun* **33**, 515–531 (2006).
16. A Schofield, P Wroth, *Critical State Soil Mechanics.* (McGraw-Hill, London), (1968).
17. B Andreotti, Y Forterre, O Pouliquen, *Granular media: between fluid and solid.* (Cambridge University Press), (2013).
18. M Schröter, S Nägle, C Radin, HL Swinney, Phase transition in a static granular system. *Europhys. Lett. (EPL)* **78**, 44004 (2007).
19. T Brzinski III, P Mayor, D Durian, Depth-dependent resistance of granular media to vertical penetration. *Phys. Rev. Lett.* **111** (2013).
20. L Roth, E Han, H Jaeger, Intrusion into granular media beyond the quasistatic regime. *Phys. Rev. Lett.* **126** (2021).
21. L Roth, Constant speed penetration into granular materials: drag forces from the quasistatic to inertial regime. *Granul. Matter* **23**, 54 (2021).
22. F Qian, D Lee, G Nikolich, D Koditschek, D Jerolmack, Rapid in situ characterization of soil erodibility with a field deployable robot. *J. Geophys. Res. Earth Surf.* **124**, 1261–1280 (2019).
23. W Kang, Y Feng, C Liu, R Blumenfeld, Archimedes' law explains penetration of solids into granular media. *Nat. Commun.* **9** (2018).
24. Y Feng, R Blumenfeld, C Liu, Support of modified archimedes' law theory in granular media. *Soft Matter* **15** (2019).
25. S Zhao, T Evans, X Zhou, Effects of curvature-related dem contact model on the macro- and micro-mechanical behaviours of granular soils. *Géotechnique* **68**, 1085–1098 (2018).
26. T Zhang, DI Goldman, The effectiveness of resistive force theory in granular locomotion. *Phys. Fluids* **26**, 101308 (2014).
27. J Ruck, et al., Downslope weakening of soil revealed by a rapid robotic rheometer. *Geophys. Res. Lett.* **51** (2024).
28. S Roux, F Radjai, *Texture-Dependent Rigid-Plastic Behavior.* (Springer Netherlands), pp. 229–236 (1998).
29. R Albert, MA Pfeifer, AL Barabási, P Schiffer, Slow drag in a granular medium. *Phys. Rev. Lett.* **82**, 205–208 (1999).
30. JM Long-Fox, ZA Landsman, PB Easter, CA Millwater, DT Britt, Geomechanical properties of lunar regolith simulants lhs-1 and lms-1. *Adv. Space Res.* **71**, 5400–5412 (2023).
31. C Li, T Zhang, DI Goldman, A terradynamics of legged locomotion on granular media. *Science* **339**, 1408–1412 (2013).
32. P Umbanhowar, D Goldman, Granular impact and the critical packing state. *Phys. Rev. E* **82** (2010).
33. R Kozlowski, H Zheng, KE Daniels, JES Socolar, Stick-slip dynamics in a granular material with varying grain angularity. *Front. Phys.* **Volume 10 - 2022** (2022).
34. LA Taylor, HH Schmitt, WD Carrier, M Nakagawa, The lunar dust problem: From liability to asset in *Proceedings of the 1st Space Exploration Conference: Continuing the Voyage of Discovery.* (American Institute of Aeronautics and Astronautics), pp. 71–78 (2005).
35. J Yang, L Wei, Collapse of loose sand with the addition of fines: The role of particle shape. *Géotechnique* **62**, 1111–1125 (2012).
36. V Trappe, V Prasad, L Cipelletti, P Segre, D Weitz, Jamming phase diagram for attractive particles. *Nature* **411** (2001).

37. NASA Solar System Exploration Research Virtual Institute (SSERVI), Nasa sservi regolith and surface testbeds (https://sservi.nasa.gov/testbed/) (year?) Accessed: 2025-05-04.
38. JK Mitchell, et al., Soil-mechanics experiments in *Apollo 15 Preliminary Science Report*, NASA Special Publication. (NASA) Vol. SP-289, (1972).
39. JK Mitchell, et al., Soil mechanics in *Apollo 16 Preliminary Science Report*, NASA Special Publication. (NASA) Vol. SP-315, (1972).
40. JK Mitchell, et al., Mechanical properties of lunar soil: Density, porosity, cohesion, and angle of friction in *Proceedings of the 3rd Lunar Science Conference.* pp. 3235–3253 (1972).
41. JK Mitchell, LG Bromwell, WDI Carrier, NC Costes, RF Scott, Soil mechanics experiment in *Apollo 14 Preliminary Science Report*, NASA Special Publication. (NASA) Vol. SP-272, pp. 87–108 (1971).
42. AK Leonovich, et al., Studies of lunar ground mechanical properties with the self-propelled lunokhod-1 in *Peredvizhnaya Laboratoriya na Luna—Lunokhod-1 ('Lunokhod 1'—Mobile Lunar Laboratory).* (Nauka, Moscow), pp. 120–135 (1971).
43. AK Leonovich, et al., Investigations of the mechanical properties of the lunar soil along the path of lunokhod i in *COSPAR Space Research XII.* (Akademie-Verlag, Berlin), pp. 53–64 (1972).
44. JE Colwell, S Batiste, M Horányi, S Robertson, S Sture, Lunar surface: Dust dynamics and regolith mechanics. *Rev. Geophys.* **45**, RG2006 (2007).
45. ZH Chen, et al., The contact force between lunar-based equipment and lunar soil. *iScience* **27** (2024).
46. OR Walton, Adhesion of lunar dust, (NASA Glenn Research Center), Contractor Report (NASA/CR–2007–214685) NASA/CR-2007-214685 (2007).
47. G Korvin, *Coordination Number of Grains.* (Springer Nature Switzerland, Cham), pp. 207–227 (2024).
48. T Majmudar, M Sperl, S Luding, R Behringer, The jamming transition in granular systems. *Phys. Rev. Lett.* **98** (2007).
49. T Aste, M Saadatfar, T Senden, Local and global relations between the number of contacts and density in monodisperse sphere packs. *J. Stat. Mech. Theory Exp.* (2006).
50. HA Makse, N Gland, DL Johnson, LM Schwartz, Why effective medium theory fails in granular materials. *Phys. Rev. Lett.* **83**, 5070–5073 (1999).
51. V Magnanimo, L La Ragione, JT Jenkins, P Wang, HA Makse, Characterizing the shear and bulk moduli of an idealized granular material. *Europhys. Lett.* **81**, 34006 (2008).
52. I Agnolin, JN Roux, Internal states of model isotropic granular packings. iii. elastic properties. *Phys. Rev. E* **76**, 061304 (2007).
53. TM Evans, JR Valdes, The microstructure of particulate mixtures in one-dimensional compression: numerical studies. *Granul. Matter* **13**, 657–669 (2011).
54. J Park, JC Santamarina, Revised soil classification system for coarse-fine mixtures. *J. Geotech. Geoenvironmental Eng.* **143**, 04017039 (2017).
55. J Kirby, M O'Sullivan, J Wood, Estimating critical state soil mechanics parameters from constant cell volume triaxial tests. *Eur. J. Soil Sci.* **49**, 85–93 (1998).
56. S Fazekas, J Török, J Kertész, Critical packing in granular shear bands. *Phys. Rev. E* **75**, 011302 (2007) Epub 2007 Jan 3.
57. F Qian, et al., Principles of appendage design in robots and animals determining terradynamic performance on flowable ground. *Bioinspiration Biomimetics* **10**, 056014 (2015).
58. F Qian, et al., Ground robotic measurement of aeolian processes. *Aeolian Res.* **27**, 1–11 (2017).
59. H Kolvenbach, et al., Traversing steep and granular martian analog slopes with a dynamic quadrupedal robot. *Field Robotics* **2**, 910 – 939 (2022).
60. S Roberts, D Koditschek, Virtual energy management for physical energy savings in a legged robot hopping on granular media. *Front Robot AI* **8**, 2296–9144 (2021).
61. J Aguilar, D Goldman, Robophysical study of jumping dynamics on granular media. *Nat. Phys* **12**, 278–283 (2016).
62. KR Fisher, et al., LASSIE: Legged Autonomous Surface Science In Analogue Environments in *54th Lunar and Planetary Science Conference.* (Lunar and Planetary Institute, The Woodlands, TX, USA), (2023) NASA Technical Reports Server Document ID: 20230000243.
63. D Jerolmack, K Daniels, Viewing earth's surface as a soft-matter landscape. *Nat Rev Phys* **1**, 716–730 (2019).
64. S Pradeep, P Arratia, D Jerolmack, Origins of complexity in the rheology of soft earth suspensions. *Nat. Commun.* **15**, 7432 (2024).
65. S Pradeep, et al., Soft matter mechanics of baseball's rubbing mud. *Proc. Natl. Acad. Sci. United States Am.* **121**, e2413514121 (2024).
66. E Fulcher, et al., Making every step an experiment: Proprioceptive sensing during locomotion for enhanced mobility and data collection in planetary-analogue explorations in *55th Lunar and Planetary Science Conference.* (Lunar and Planetary Institute, The Woodlands, TX, USA), Vol. 55, (2024).
67. G Kenneally, D Koditschek, Leg design for energy management in an electromechanical robot. *2015 IEEE/RSJ Int. Conf. on Intell. Robots Syst.* pp. 5712–5718 (2015).
68. G Kenneally, D Koditschek, Design principles for a family of direct-drive legged robots. *IEEE Robotics Autom. Lett.* **1**, 900–907 (2016).
69. J Ruiz-Suárez, Penetration of projectiles into granular targets. *Reports on Prog. Phys.* **76**, 066601 (2013).

Supporting Information for

Unified Granular Intrusion Dynamics for Planetary Materials

John G. Ruck, Shravan Pradeep, John C. Bush, Eric D. Sigg, Feifei Qian, Douglas J. Jerolmack

Douglas J. Jerolmack
E-mail: sediment@sas.upenn.edu

This PDF file includes:

Supporting Information Text

S1. Derivation for the expression of strain from the Critical State Soil Mechanics (CSSM) framework. Critical State Soil Mechanics (CSSM) framework proposes the following relationship between the evolution of solid volume fraction (ϕ) and the total system strain (γ) (1).

$$\frac{d\phi}{d\gamma} = -\phi \tan(n(\phi - \phi_c))$$

Here, ϕ_c is the critical volume fraction. We can start by integrating the above expression to obtain the strain (γ) as a function of the granular volume fraction (ϕ):

$$\int d\gamma = \int \frac{-1}{\phi \tan(n(\phi - \phi_c))}\, d\phi = -\int \frac{\cot(n(\phi - \phi_c))}{\phi}\, d\phi$$

Since the integral on the right does not have a closed form solution, we can use Taylor series expansion around $\phi = \phi_c$. This is a reasonable assumption in our case since we are investigating the behavior of system around the critical point ϕ_c, as the system move towards it. Therefore, mathematically we can define a distance to critical parameter $\Delta\phi = \phi - \phi_c$. Then, the Taylor series for $\cot(n(\Delta\phi))$ around $\Delta\phi = 0$ can be written as:

$$\cot(n\Delta\phi) = \frac{1}{n\Delta\phi} - \frac{n\Delta\phi}{3} + \mathcal{O}(\Delta\phi^3)$$

Now higher-order expansions of $\Delta\phi$ values are small. Bringing it back to the mathematical form of the right side integrand and expanding $\Delta\phi$ and we can approximate the system strain (γ) to the first order term as:

$$\gamma \approx -\int \frac{1}{\phi}\left[\frac{1}{n(\phi - \phi_c)}\right] d\phi = -\frac{1}{n\phi_c}\int \left[\frac{1}{(\phi - \phi_c)} - \frac{1}{\phi}\right] d\phi$$

Now evaluating the integrands we have:

$$\gamma \approx \frac{-1}{n\phi_c}\int \frac{1}{\phi(\phi - \phi_c)} d\phi = \frac{-1}{n\phi_c}\int \frac{1}{\phi - \phi_c} d\phi - \int \frac{1}{\phi} d\phi = \frac{-1}{n\phi_c}\left(\ln|\phi - \phi_c| - \ln|\phi|\right) + C_1 = \frac{-1}{n\phi_c}\ln\left|\frac{\phi - \phi_c}{\phi}\right| + C_1$$

As, the system evolves from $\phi \to \phi_c$, the maximum deformation is $\approx -1/n\phi_c$ (1). This gives us the constact of intergration, $C_1 \approx \frac{-1}{\phi_c}$. Since $\phi = \phi_c$ is small we can further use Taylor expansion to the natural log term as $\ln\left|\frac{\phi - \phi_c}{\phi}\right| = \ln\left|1 - \frac{\phi_c}{\phi}\right| = -\phi_c/\phi$ + higher order terms. Further simplifying the parameters from experimental data fit, the denominator $n\phi_c \sim \mathcal{O}(1)$. Combining all these, the total strain γ can be written as:

$$\gamma \sim \left(1 + \ln\left|\frac{\phi - \phi_c}{\phi}\right|\right) \sim \left(1 + \frac{-\phi_c}{\phi}\right)$$

OR

$$\gamma \equiv \frac{\phi - \phi_c}{\phi}$$

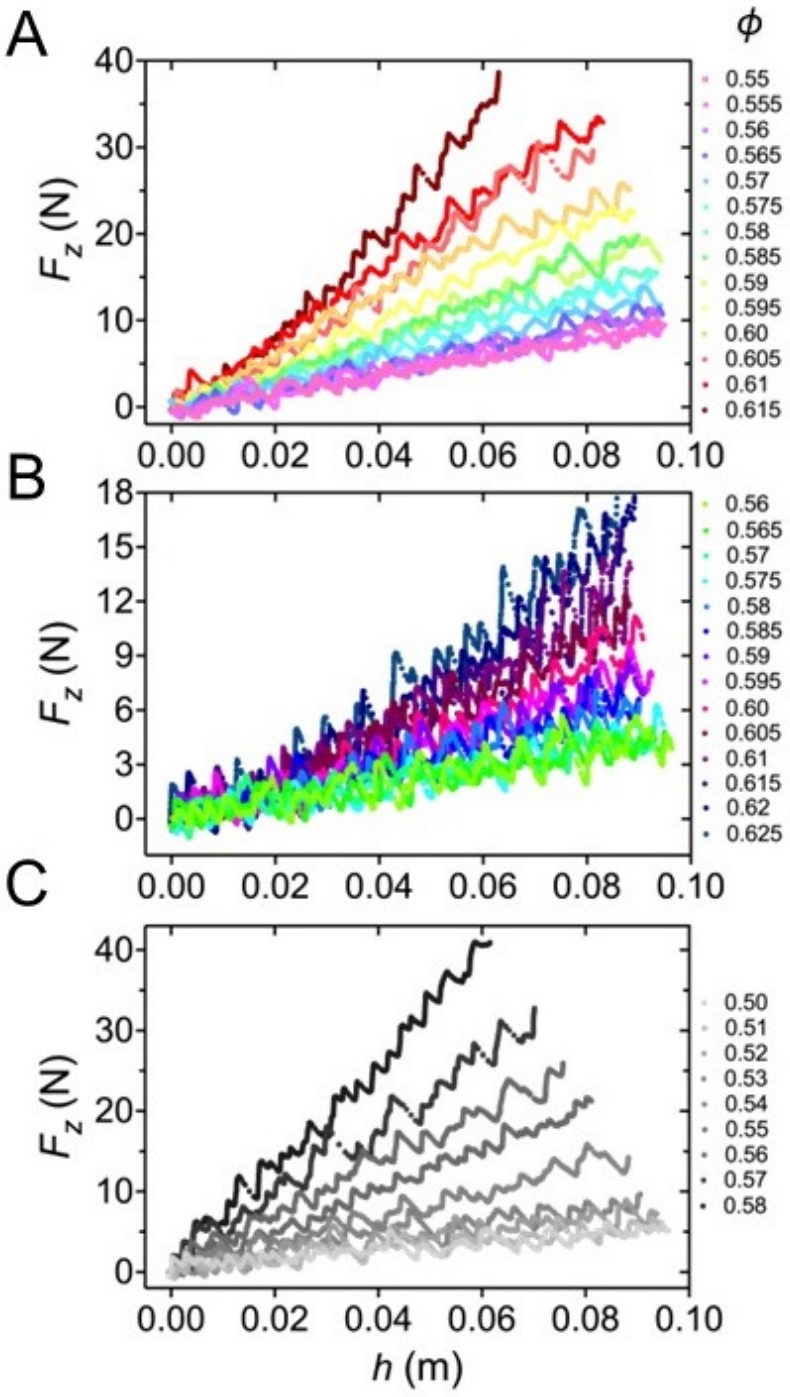

Fig. S1. Force-depth curves from intrusion tests into frictional materials. (A) An average profile of four tests into sand, (B) glass beads, and (C) LHS-1 without fines.

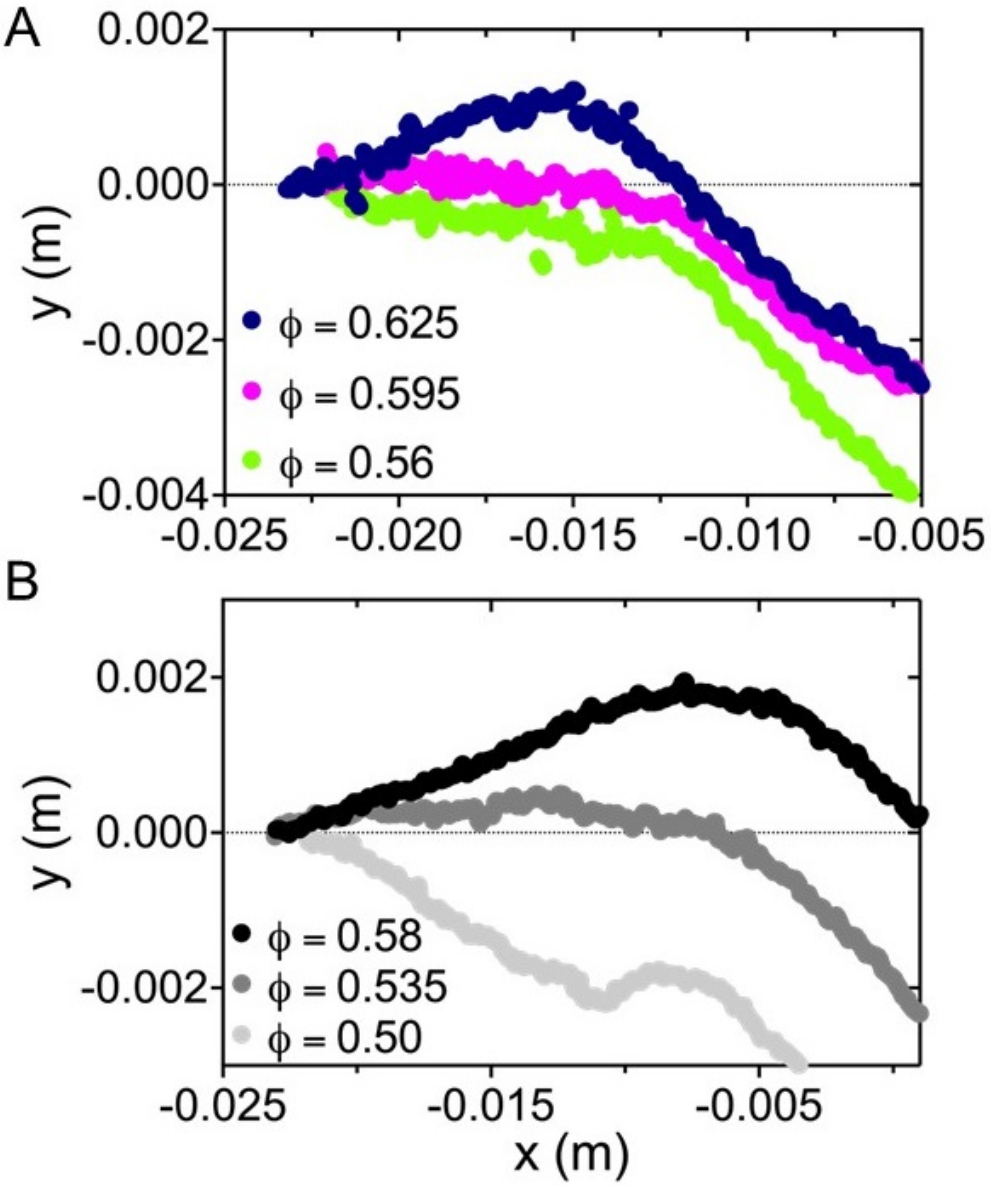

Fig. S2. Topography measured using the laser line profilometer during intrusion tests at ϕ_{min}, ϕ_c, and ϕ_{max} for (A) glass beads and (B) LHS-1 without fines.

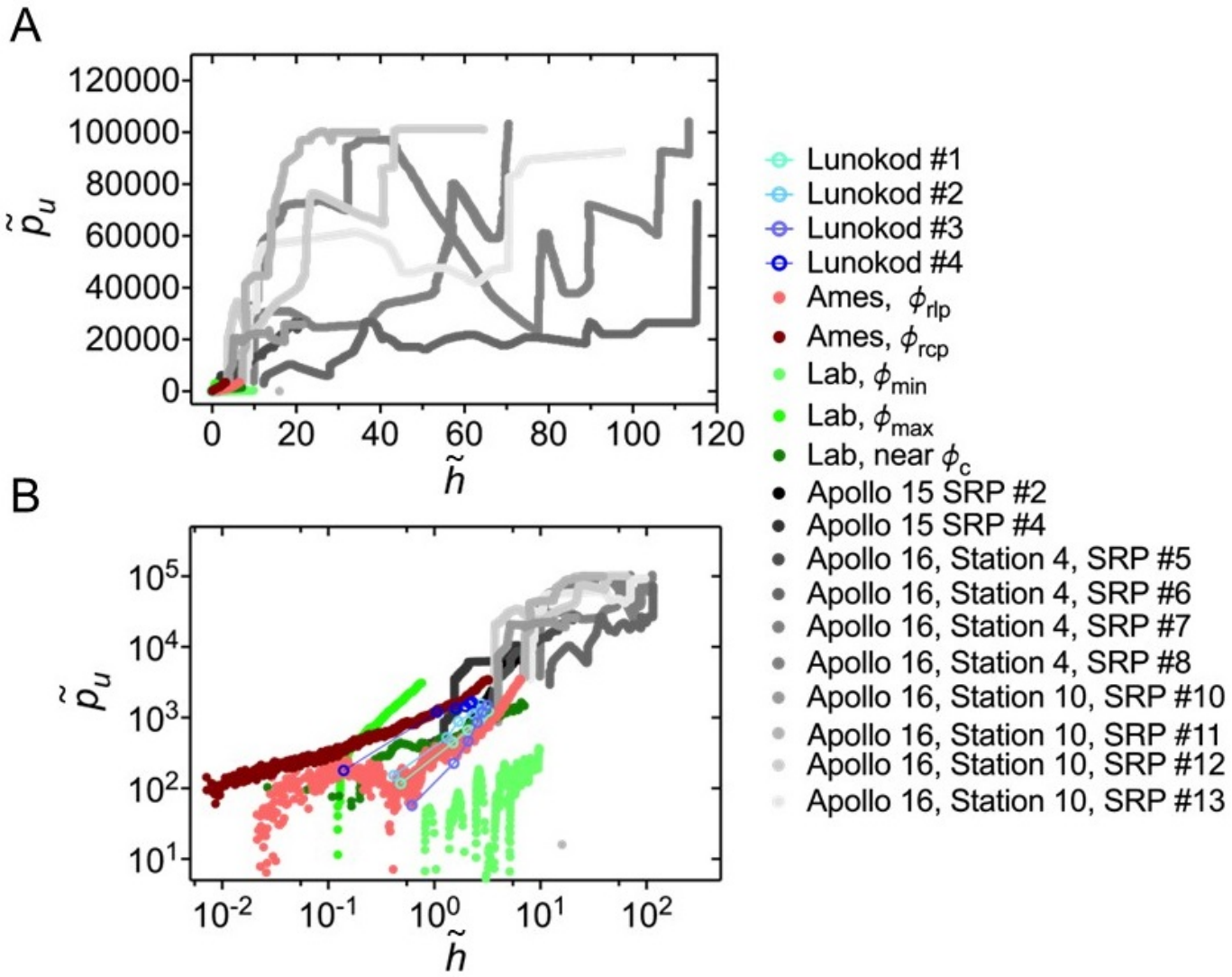

Fig. S3. All of the reinterpreted penetration data from the lunar surface and laboratory experiments into lunar simulant. (A) Dimensionless pressure-depth plots from penetration into lunar regolith from Apollo 15 & 16 and Lunokhod 1, as well as LHS-1 in both the laboratory and the NASA Ames SSERVI test bed. (B) Dimensionless pressure-depth data plotted in log-log space.

References

1. B Andreotti, Y Forterre, O Pouliquen, *Granular media: between fluid and solid*. (Cambridge University Press), (2013).